# Journal of Materials Chemistry A

Accepted Manuscript


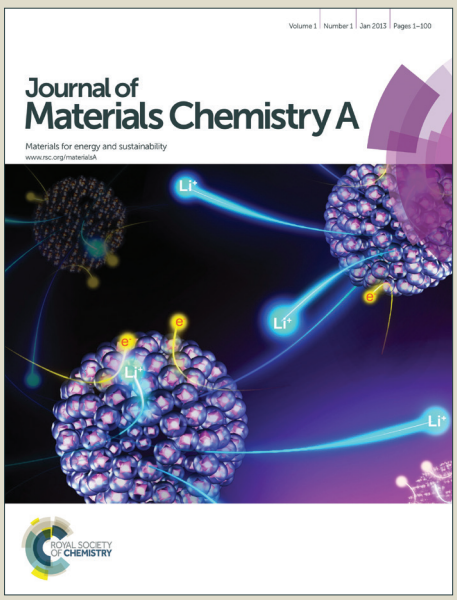





ROYAL SOCIETY OF CHEMISTRY

www.rsc.org/materialsA

Table of contents

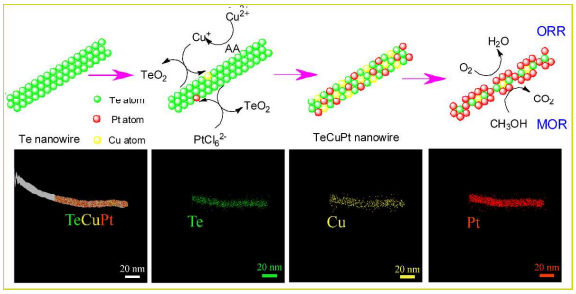


Alloying Pt with both Te and Cu could effectively improve ternary TeCuPt catalytic activity for electronic and geometric structure effects.

# Te–template approach to fabricating ternary TeCuPt alloy nanowires with enhanced catalytic performance towards oxygen reduction reaction and methanol oxidation reaction

Haibo Li,*[a] Cancan Ren,[a] Shuling Xu,[a] Lei Wang,[a] Qiaoli Yue,[a] Rui Li,[a] Yuanfu Zhang,[a] Qingwang Xue,[a] and Jifeng Liu*[ab]

[a]Department of Chemistry, Liaocheng University, Liaocheng 252059, PR China

[b]Key Laboratory of Food Nutrition and Safety, Ministry of Education of China, Tianjin University of Science and Technology, Tianjin 300457, China

## Abstract

Fabricating ternary Pt-based alloys has emerged as a promising strategy to further enhance the catalytic performance of Pt catalyst in direct methanol fuel cell (DMFC) for both oxygen reduction reaction (ORR) and methanol oxidation reaction (MOR). Herein we reported for the first time the synthesis of ternary TeCuPt nanowires (NWs) by a Te-template-directed galvanic replacement reaction, in which Te NWs served as both sacrificial templates and reducing agents. Compared with binary TePt alloy and pure Pt catalysts, the ternary TeCuPt alloys exhibited a more positive half-wave potential and higher specific area/mass activity for ORR, and it also displayed a better CO tolerance ability and long-term stability for MOR. The enhanced catalytic performance for TeCuPt NWs was attributed to the electronic and geometric structure effects, originating from the Pt alloying with both Te and Cu components, which could weaken the binding strength between Pt surface atoms and intermediate species (e.g. OH*, CO*). Our studies demonstrated a new alternative ternary Pt-based catalyst

for both ORR and MOR, and it may find application in DMFC.

## Introduction

Direct methanol fuel cell (DMFC) represents one of the most promising alternatives to traditional power sources. However, its commercialization is still seriously hampered by the low performance and high cost of Pt catalyst, which catalyzes the oxygen reduction reaction (ORR) at the cathode and the methanol oxidation reaction (MOR) at the anode of DMFC. To overcome above obstacle, shape-controlled Pt nanocrystals have been extensively studied by finely modulating surface Pt atom arrangement. For example, polyhedral Pt nanocrystals enclosed by high-index facets (*e.g.* {910}, {730}, {520}) exhibited an enhanced catalytic activity for equivalent Pt.[1–3] Supporting small-size Pt nanoparticles with graphitic carbon (nitride),[4–7] titanium/vanadium nitride (Ti/VN),[8, 9] and titanium/niobium carbide (Ti/NbC)[10, 11] can also obtain a high electrochemical activity whilst the Pt loading can be highly reduced. Besides, covering the surface of other metal with a thin (ideally monolayer) Pt, *i.e.* a core–shell structure, can greatly enhance the specific activity of Pt catalyst,[12–16] because majority of Pt atoms are distributed at the electrochemical reaction interface.

Nowadays, a consensus has been approved that some intermediates, such as the OH* for ORR and the CO* for MOR (where * denotes an adsorbed species), can occupy Pt active sites, and therefore hinder Pt catalytic utility. Great efforts have been devoted to fabricating binary Pt-based alloys by introducing a transition metal (M = Fe, Co, Ni, Cu, *etc*),[17–21] and these Pt–M binary alloys exhibit a superior catalytic performance compared with pure Pt. The enhanced catalytic activity for Pt-based

alloys was generally attributed to the electronic (Pt d-band vacancy) and geometric (Pt-Pt bond distance) modulation.[22, 23] In binary Pt-based alloys, the incorporation of transition metal can modify Pt electronic structure due to the electron transfer from M to Pt, and it can also cause a lattice contraction, resulting in a more favorable Pt–Pt distance. Above effects will highly alter the binding strength between the Pt surface atoms and the intermediate products (*e.g.* OH*, CO*) and further influence Pt catalytic activity.[24]

Compared with binary Pt–M alloys, ternary Pt-based alloys exhibit a much higher catalytic performance. Recent studies have proved that the ternary FePtCu alloy had much better ORR catalytic activity and stability than the commercial Pt/C and binary FePt catalysts.[25] It has also been reported that the ternary FePtRu outperformed the binary FePt and PtRu in terms of catalytic activity and CO tolerance ability in MOR.[26] To obtain ternary Pt-based alloys, synthesis approaches, including plasma co-sputtering,[27] impregnation–reduction–annealing,[28] underpotential electrodeposition,[29] coreduction Pt- and M-based precursors in aqueous solution,[30] and organic solvent [25, 31] (*e.g.* oleylamine and oleic acid) have been widely adopted. Recently, template-directed galvanic replacement reaction has also been developed to prepare ternary Pt-based alloys from single metal, which serves as both template and reducing agent. For example, ternary PtPdCu nanotubes (NTs) and PtPdTe nanowires (NWs) have been successfully prepared with Cu and Te NWs as templates, respectively.[23, 32]

In present work, we reported for the first time the synthesis of ternary TeCuPt

NWs by a Te-template-directed galvanic replacement reaction, and further investigated their catalytic utility towards both ORR and MOR. In this method, Te NWs served as both sacrificial templates and reducing agents for the formation of TeCuPt NWs. Alloying Pt with both Te and Cu highly reduced Pt d-band center owing to the electronic and geometric effects, which weakened the binding strength between Pt surface atoms and OH*/CO* intermediate species, and therefore the Pt catalytic performance towards both ORR and MOR was evidently improved.

## Experimental section

### Chemicals and materials

The following reagents were used: sodium tellurite ($Na_2TeO_3$, 97.0 %), cetyltrimethylammonium bromide (CTAB, 99.0 %), ascorbic acid (AA, 99.7 %), $H_2PtCl_6{\cdot}6H_2O$ (37.5 % Pt), $CuSO_4{\cdot}5H_2O$ (99.0 %), sulfuric acid (98.0 %), methanol (99.9 %), absolute ethanol (99.7 %). All chemicals were used without further purification. All solutions used in electrochemical tests were well prepared with Millipore-Q water (≥ 18.2 MΩ).

### Synthesis of metallic Te NWs

Te NWs were prepared following Qian's work.[33] Briefly, 1.0 g AA and 0.1 g CTAB were added to a 50 mL Teflon-lined autoclave filled with 40 mL distilled water, and then 0.052 g $Na_2TeO_3$ was added to the solution under vigorous stirring. The sealed vessel was maintained at 90 °C in an oven for 10 h. Finally, the well-dispersed Te NW suspension, without any further treatment, was stored in a glass bottle for the following process.

**Synthesis of ternary TeCuPt NWs and binary TePt NTs**

The synthesis for TeCuPt NWs followed: 20 mL Te NW suspension as mentioned above was transferred to a round flask with a capacity of 50 mL. Then, 1.2 mL $CuSO_4$ (50 mM) and 1.2 mL $H_2PtCl_6$ (50 mM) was slowly (taking 30 min) injected to the solution at a rate of 0.67 μL/s by a peristaltic pump (Model: LSP04-01A, Baoding Longer Precision Pump Co., Ltd). The mixed-solution was further stirred for 2 h at room temperature, and then 1.6 g KOH was added to remove the residual Te. The final precipitate was collected by centrifugation, washed with distilled water and ethanol, and then dried at a vacuum atmosphere. The synthesis for TePt NTs was similar with the case of TeCuPt NWs except for the absence of 1.2 mL $CuSO_4$ (50 mM).

**Material characterization**

The phase identification was accomplished by powder X-ray diffraction (XRD) employing a Philips X'pert X-ray diffractometer with Cu Kα radiation (λ =1.5418 Å). The transmission electron microscopy (TEM) and high-resolution transmission electron microscopy (HRTEM) were performed on a JEOL JEM-2100 or JEM-ARM200F transmission electron microscope at an accelerating voltage of 200 kV. The scanning electron microscopy (SEM) was performed on a Zeiss Supra-40 scanning electron microscope with an accelerating voltage of 5 kV. Element distribution mapping and linear scan were performed by high-angle annular dark-field scanning TEM-energy-dispersive X-ray spectroscopy (HAADF-STEM-EDS) with an Oxford INCA energy dispersive X-ray detector equipped on JEM-ARM200F transmission electron microscope. X-ray photoelectron spectroscopy (XPS) study was

performed on an ESCLAB MKII X-ray photoelectron spectrometer.

**Electrochemical measurements**

All electrochemical tests were conducted on a CHI 832B potentiostat (Shanghai Chenhua Co., China) in a standard three-electrode system with a coiled platinum wire ($\Phi$ = 0.5 mm, $L$ = 23 cm ) and an Ag/AgCl (3M NaCl) electrode as the counter and reference electrodes, respectively. The working electrode was a glassy carbon rotating disk electrode (RDE, ALS Co., Ltd) and its geometric area is 0.1256 $cm^2$. All potentials in this work were converted to the reversible hydrogen electrode (RHE) via Nerst equation: $E_{RHE} = E_{Ag/AgCl} + 0.059\ pH + E^{o}_{Ag/AgCl}$. Before each test, the RDE surface was polished with 0.05 μm alumina paste until a mirror-finish surface was obtained, and then it was fully rinsed with water. The working electrode was fabricated by coating catalyst ink at the same metal loading by weight (16 μg). Typically, 4 μL (4 mg/mL) well-dispersed catalyst suspension (TeCuPt NWs, TePt NTs, and Pt black (JM)) was coated on the electrode surface using a microsyringe and followed adding 1 μL 0.5 wt % Nafion solution (in ethanol) to cover the surface of the catalysts, then dried in flowing argon atmosphere.

The ORR and MOR catalytic performances were characterized by cyclic voltammetry (CV), linear sweep voltammetry (LSV), and chronoamperometry (CA) methods. To activate catalyst, the catalyst-coated RDE was scanned in Ar-saturated 0.50 M $H_2SO_4$ solution between 0.0 and 1.2 V at a scan rate of 0.5 V/s for 250 cycles until reaching a steady state. For ORR measurement, LSVs were recorded within the potential range of 0.3 ~ 1.0 V in $O_2$-saturated 0.05 M $H_2SO_4$ solution. For MOR

measurement, CVs were recorded within the potential range of 0 ~ 1.2 V in Ar-saturated 0.50 M $H_2SO_4$ + 1.0 M $CH_3OH$ solution. To evaluate the stability of catalysts, CAs were recorded at 0.8 V *vs.* RHE in Ar-saturated 0.50 M $H_2SO_4$ + 1.0 M $CH_3OH$ solution.

## Results and discussion

The used Te NWs for synthesis of TeCuPt NWs were prepared following Qian's work.[33] As shown in Figure 1a,b, the as-prepared Te NWs had a large length-diameter ratio. A representive Te nanowire (Figure 1c) was further characterized by HRTEM technique. The observed lattice spacings are 0.590 and 0.310 nm (Figure 1d), corresponding to the separations of (001) and (101) planes of hexagonal-phase Te (JCPDS No. 36-1452). The corresponding ED pattern further confirmed the (001) and (101) diffraction dots (inset of Figure 1d). Both the HRTEM image and ED pattern well demonstrated that the as-prepared Te NWs were single-crystalline character and grew along the [001] direction, which was well consistent with literature results.

Figure 2 shows the XRD pattern (purple curve) of as-prepared TeCuPt NWs before KOH treatment, in which two broad peaks are observed as well as one sharp peak. It should be noted that the sharp diffraction peak could be well indexed as the (101) planes of the hexagonal-phase Te (JCPDS No. 36-1452), which came from the unreacted Te. To purify the TeCuPt NWs, the product was further treated with KOH, and then the unreacted Te could be removed. As shown in Figure 2 (black curve), no obvious diffraction peak from the (101) planes of hexagonal-phase Te is found, whilst the two broad peaks (located at $2\theta$ = 31.0 and 45.6) from the TeCuPt NWs become

sharp.

The element composition of products was determined by EDS. The Fe, Mo, and C element signals came from the specimen holder and molybdenum grid, which supported the samples (Figure S1). Quantitative analysis by EDS revealed that the Te/Cu/Pt atomic ratio for ternary TeCuPt NWs was 51:12:37 (Figure S1a). The chemical state of Pt in TeCuPt NWs was examined by XPS. As shown in Figure 3a, the asymmetric Pt 4f core shell (CL) spectrum of TeCuPt NWs could be deconvoluted into two pairs of doublets due to the presence of mulriple chemical state (Figure 3b). The two peaks centered at 71.3 (Pt $4f_{7/2}$) and 74.6 (Pt $4f_{5/2}$) eV were characteristic of metallic Pt(0). The other two peaks at 72.4 (Pt $4f_{7/2}$) and 75.8 (Pt $4f_{5/2}$) eV could be assigned to the Pt(II) species in PtO and $Pt(OH)_2$. The high ratio for Pt(0)/Pt(II) implied that the Pt in TeCuPt NWs was predominantly in the zero-valent sate (Table 1).

It has been reported that the electron transfer will occur in Pt-based alloys for different electronegativity, and thus affects Pt binding energy and d-band center.[34, 35] For the metallic Pt with almost filled d-bands, the CL shift is a good indicator ("fingerprint") of the shift for the occupied d-band center.[36] Compared with the pure Pt catalysts (Figure 3a,d), an upshift of Pt 4f CL binding energy was evidently observed for the TeCuPt NWs (Figure 3a,b). In general, a positive shift of binding energy has been interpreted by an electron loss of the atom.[37] In ternary TeCuPt NWs, the metallic Pt (2.28) has a slightly higher electronegativity than both Te (2.12) and Cu (1.90), and then the electron transfer will occur from both Te and Cu to the Pt

atom. How to explain the upshift of Pt4f CL binding energy for the TeCuPt NWs? The studies by *Mukerjee et al.* have revealed that the total numbers per Pt atom increased, while the Pt 5d electron decreased when Pt being alloyed with a second component.[22] Recently, *Weinert et al.* attributed the upshift of Pt4f CL binding energy to the difference in work function between the pure Pt and Pt-based alloy, accompanied by the rehybridization of the d-band as well as the sp-band.[38] The work function change leads to the upshift of reference level, *i.e.* Fermi energy ($E_F$), in photoelectron measurement.[36] Above statements well explained the upshift of Pt4f CL binding energy in ternary TeCuPt NWs as well as the downshift of the d-band center. Besides, the upshift of Pt4f CL binding energy was also found in binary TePt NTs (Figure 3a,c), but their upshift was lower than TeCuPt NWs (Table 1). It implies that the incorporation of both Cu and Te elements can more effectively reduce Pt d-band center.

Figure 4a,b show the TEM images of ternary TeCuPt NWs before KOH treatment, which well inherit the microstructure of Te templates. Careful characterization revealed that a few of TeCuPt NWs had a core-shell structure (Figure S2a). The observed lattice spacing for the core section was 0.310 nm (inset of Figure S2a), corresponding to the separation of (101) planes of the hexagonal-phase Te (JCPDS No. 36-1452). It implied that some residual Te did not take part in the formation of ternary TeCuPt alloy. This result was consistent with the XRD pattern (Figure 2), from which the hexagonal-phase Te (101) diffraction peak was also observed. The unreacted Te core could be removed by KOH treatment, and then a few

of TeCuPt NTs were found (Figure S2b). Compared with Figure 4a,b, the TeCuPt NWs after KOH treatment still retained one-dimensional structure (Figure 4c,d), while the surface roughness became obvious (Figure 4e). It can be explained by the dissolution of residual Te induced from the KOH treatment. The HRTEM characterization revealed that the orientation of lattice fringes was random (Figure 4f and Figure S3), implying a polycrystalline character of TeCuPt NWs. The observed lattice spacings were 0.281 and 0.197 nm (Figure 4g,h), corresponding to the two diffraction peaks at $2\theta = 31.0$ and 45.6, respectively. To investigate the distribution of Te, Cu, and Pt elements, the element mapping was performed by HAADF-STEM-EDS (Figure 4i–l). It was found that the Te, Cu, and Pt elements were uniformly distributed throughout the nanowire, which unambiguously demonstrated that the as-prepared NWs were ternary alloys of Te-Cu-Pt.

When only 1.2 mL $H_2PtCl_6$ (50 mM) was added to 20 mL Te NW suspension, the Te resources were excess, so only partial Te at the outer section of NWs was consumed. As shown in Figure 5a,b, the unreacted Te at the core section of NWs could also be removed by following KOH treatment, and then binary TePt NTs were obtained. Quantitative analysis by EDS revealed that the Te/Pt atomic ratio for TePt NTs was 49: 51 (Figure S4). Careful HRTEM study revealed that the observed lattice spacing was 0.283 nm (Figure 5c–e), which was well consistent with the separation of (020) planes of the orthorhombic-phase TePt (JCPDS No. 18-976).

It should be noted that the slow injection of $CuSO_4$ and $H_2PtCl_6$ was favorable for the formation of ternary TeCuPt alloy. Comparative experiments confirmed that

the fast injection of $CuSO_4$ and $H_2PtCl_6$ resulted in the formation of small size Pt nanoparticles on the surfaces of ternary TeCuPt alloy (Figure S5a–c), which could be confirmed by the observed lattice spacing of 0.227 nm (Figure S5d,e), corresponding to the lattice spacing of *fcc*-Pt (111) plane (JCPDS No. 4-802). Similarly, the fast injection of single $H_2PtCl_6$ also leaded to the formation of small size Pt nanoparticles on the surfaces of binary TePt alloy (Figure S6).

Herein, the Te NWs served as both sacrificial templates and reducing agents for the formation of TeCuPt NWs by a galvanic replacement reaction. On the basis of Nernst equation, the electrode potential for the $TeO_2$/Te oxidation-reduction pair highly depends on the proton concentration in following reaction: $TeO_2 + 4H^+ + 4e = Te + 2H_2O$. The pH value for the Te nanowire suspension was determined to be 2.5, and then we conveniently obtained the electrode potential (0.450 V *vs.* RHE) for the $TeO_2$/Te by Nernst equation. So the $PtCl_6^{2-}$ can be facilely reduced to metallic Pt by Te for their higher electrode potential (0.718 V *vs.* RHE), however, the reduction of $Cu^{2+}$ to Cu can not be directly realized by Te for their lower one (0.342 V *vs.* RHE). How is the $Cu^{2+}$ been reduced to Cu? It should be noted that the residual ascorbic acid, which was highly excess for the reduction of $Na_2TeO_3$, in Te NW suspension plays a crucial role. According to the *Warner's* study,[39] the reduction of $Cu^{2+}$ ion in the presence of ascorbic acid will result in the formation of $Cu^+$ ion (Figure S7 and S8), which can be further reduced to Cu (Figure S9) by Te for its higher electrode potential (0.521 V *vs.* RHE). The above reactions can be summarized as follows:

$$PtCl_6^{2-} + Te + 2H_2O \rightarrow Pt + TeO_2 + 4H^+ + 6Cl^-$$

$$Cu^{2+} \xrightarrow{AA} Cu^+$$

$$4Cu^+ + Te + 2H_2O \rightarrow 4Cu + TeO_2 + 4H^+$$

$$Pt + Cu + Te \rightarrow TeCuPt$$

The Scheme 1 illustrates the formation process of ternary TeCuPt NWs.

To activate catalysts, the dealloying process was realized by repetitive CV scans for 250 cycles in Ar-staturated 0.5 M $H_2SO_4$. As shown in Figure 6a, the first cycle CV for TeCuPt NWs showed no hydrogen adsorption in the potential range of 0 ~ 0.35 V, while two anodic peaks were found. Compared with the pure Pt (JM) catalysts (Figure 6b), the anodic peak at 0.35 ~ 0.55 V could be attributed to the dissolution of Cu atoms from the TeCuPt NWs,[23, 28, 40] and another one at 0.55 ~ 0.80 V resulted from the dissolution of Te atoms from the TeCuPt NWs. In the following cycling, the intensity for anodic peaks decreased, and simultaneously the underpotential hydrogen adsorption/desorption peaks increased, implying the formation of Pt exposure surfaces. After 150 cycles, the peak position and intensity did not change, implying the formation of a stable Pt surface.

Previous study has proved that elecrochemical dealloying was a key process to improve the catalytic activity of Pt–based binary or ternary alloys by generating Pt-enriched shells.[25, 41] For TeCuPt NWs, the EDS quantitative analysis revealed that the Te/Cu/Pt atomic ratio changed from the 51:12:37 to 8:4:88 (Figure S1b), and it well confirmed the partial removal of Te, Cu atoms from alloys. We also investigated the microstructure variation of TeCuPt NWs after dealloying process. As shown in

Figure 7a,b, the ternary TeCuPt alloy still retained the wire-like morphology and polycrystalline character (Compared with the TeCuPt NWs, evidently structure change, from tube-like to branched zigzag structure (Figure S10), was observed for TePt NTs after CV dealloying). The observed lattice spacings were 0.224 and 0.195 nm (Figure 7c,d), being close to the separations of (111) and (200) planes of *fcc*-Pt (JCPDS No. 4-802), respectively. It implied that a phase transformation from orthorhombic lattice to cubic one may occur during the dealloying process. We believed that the above phase change was induced by the severe leaching of Te component with the atomic fraction decreasing from 51 % to 8 %, followed by the arrangement of Pt atoms for more favorable crystallographic facet and Pt–Pt distance.[41] As shown in Figure 7e–i, the HAADF-STEM-EDS element mapping and linear scan revealed that the Pt was evenly distributed across the NW while the Te and Cu populated inside the NW, implying the formation of Pt-enriched surfaces after dealloying process.

The electrochemical active surface area (ECSA) was calculated from the total charge of the $H_{upd}$ desorption by adopting an assumption of 210 μC/cm$^2$ corresponding to the adsorption of a hydrogen monolayer.[42] The calculated ECSAs for TeCuPt NWs, TePt NTs, and pure Pt catalysts were 20.1, 15.5, and 14.2 m$^2$/g, respectively (Figure 8a). The electrocatalytic performances towards ORR for TeCuPt NWs，TePt NTs, and pure Pt catalysts were characterized using RDE, and the polarization curves (Figure 8b) were recorded in $O_2$-saturated 0.05 M $H_2SO_4$ solution. It was found that TeCuPt NWs showed a more positive half-wave potential ($E_{1/2}$)

(0.83 V *vs.* RHE) than both TePt NTs (0.82 V *vs.* RHE) and pure Pt catalysts (0.80 V *vs.* RHE). To well evaluate the intrinsic activity of catalysts, the specific area activity ($J_{area}$) and mass activity ($J_{mass}$) of Pt were obtained by normalizing the kinetic current ($I_k$) by the ECSA and total mass of Pt on the electrode, respectively. The value (Figure 8c) of kinetic current ($I_k$) at kinetic-controlled region was obtained from the polarization curve according to the Koutecky–Levich (K–L) equation: [42]

$$I_k = \frac{I \times I_L}{I_L - I}$$

where $I$, $I_k$, $I_L$ represented the measured, kinetic, and diffusion-limited current, respectively. As shown in Figure 8d, the specific area activity ($J_{area}$) for TeCuPt NWs at half-wave potential (0.83 V *vs.* RHE) was 0.29 $mA/cm^2_{Pt}$, which was higher than that for TePt NTs (0.25 $mA/cm^2_{Pt}$) and pure Pt catalysts (0.11 $mA/cm^2_{Pt}$). The specific mass activity for TeCuPt NWs (59 $mA/mg_{Pt}$) was also higher than that for TePt NTs (44 $mA/mg_{Pt}$) and pure Pt catalysts (16 $mA/mg_{Pt}$). Therefore, TeCuPt NWs outperformed both TePt NTs and pure Pt catalysts towards catalyzing ORR in terms of half-wave potential ($E_{1/2}$), specific area activity ($J_{area}$) and mass activity ($J_{mass}$) (Table 2). So it could be concluded that the introduction of both Te and Cu elements into Pt could effectively enhance ORR catalytic performance compared with binary TePt alloy and pure Pt catalysts.

It is well known that ORR process involves both the O–O bond dissociation and the surface OH* group removal as the basic elementary steps for a 4-electron reduction path.[35] For Pt-based catalysts, the high coverage of intermediate OH* on Pt active sites will block $O_2$ molecule adsorption, so the OH* removal from Pt surface is

usually a rate-limiting step and highly determines the ORR catalytic activity.[23, 43] As shown in Figure 8a, the OH* stripping peak for TeCuPt NWs is located at a potential (~ 760 mV *vs.* RHE) higher than that of TePt NTs (~ 748 mV *vs.* RHE) and pure Pt (JM) catalysts (~ 743 mV *vs.* RHE). The positive shift for the OH* stripping peak implies a weaker Pt–OH* interaction on the TeCuPt NWs with respect to that for TePt NTs and pure Pt catalysts,[35] and it will facilitate the removal of OH* group and the renewal of Pt active sites, giving rise to a higher ORR catalytic activity for TeCuPt NWs. According to previous study, the strength of coupling between the OH* and the Pt surface can be weakened when Pt d-band center is far from the $E_F$.[23, 24] For the TeCuPt NWs, the downshift of Pt d-band center can be interpreted by considering the electronic and geometric structure effects. On the one hand, the incorporation of both Te and Cu atoms can modify Pt electronic band structure, which has been detailed discussed in above XPS section (Figure 3b);[44] on the other hand, it also causes a compressive strain for surface Pt atoms. Compared with Pt (1.39 Å) atom, both Te (1.37 Å) and Cu (1.28 Å) atoms have smaller atomic sizes. So the Pt overlayers of TeCuPt NWs have a shortened Pt–Pt interatomic distance than pure Pt, which could be confirmed by the shortened lattice spacings of 0.224 and 0.195 nm for (111) and (200) planes, respectively (Figure 7c,d). Such a compressive strain would cause a downshift of d-band center of surface Pt atoms according to *Chen's* study.[12]

We also examined the MOR catalytic activity of TeCuPt NWs and TePt NTs, and the pure Pt catalysts were also given for comparison (Table 2). The catalytic activity for MOR was evaluated by CVs in Ar-saturated 0.50 M $H_2SO_4$ + 1.0 M $CH_3OH$

solution, and the oxidation current density was normalized by the Pt mass. During MOR process, it usually involves the adsorption of methanol molecules on catalyst surface, dehydrogenation of methanol molecule to CO* species, and the further oxidation of CO* to final product of $CO_2$.[45] The formation of CO* intermediates will significantly block methanol molecule access to the Pt active sites, reducing the catalytic activity of Pt-based catalyst.[8] As shown in Figure 9a, the oxidation current density ($J_f$) of the forward sweep, corresponding to the methanol oxidation, was recorded to be 245, 223, and 105 mA/$mg_{Pt}$ for TeCuPt NWs, TePt NTs and pure Pt (JM) catalysts, respectively. The $J_f$ value for the TeCuPt NWs was higher than that of TePt NTs and pure Pt catalysts, indicating a higher efficiency for methanol oxidation. The current density ($J_b$) of the backward sweep, corresponding to the oxidation of CO*,[45] was also recorded, and the value of $J_f/J_b$ was applied to evaluate the poisoning tolerance of catalysts. Generally, a higher $J_f/J_b$ suggests a higher resistance to the CO*. The $J_f/J_b$ for the TeCuPt NWs, TePt NTs, and pure Pt (JM) catalysts were 1.10, 1.00, and 0.90, respectively. Compared with the TePt NTs and pure Pt catalysts, the TeCuPt NWs exhibited a better CO tolerance ability, which resulted from the decreased CO bonding strength for the downshift of Pt d-band center position.[24]

To evaluate the long-term stability of catalysts, a CA test at a constant potential of 0.8 V *vs.* RHE was conducted in Ar-saturated 0.50 M $H_2SO_4$ + 1.0 M $CH_3OH$ solution (Figure 9b). At the initial stage, the CAs generated high charging currents due to the high concentration of methanol molecules on the catalyst surface. The following current decay mainly resulted from the inhibition of surface reaction active

sites by accumulated CO* poisoning specie and $SO_4^{2-}$ adsorption on the catalyst surface. The CA curves clearly indicated that the TeCuPt NWs had a much higher current density over the entire time range, with a much slower current decay rate among the three catalysts. The enhanced catalytic durability of TeCuPt was attributed to its superior CO antipoisoning performance.

## Conclusions

Ternary TeCuPt NWs were fabricated by Te-template-directed galvanic replacement reaction, and they exhibited an enhanced catalytic performance towards both ORR and MOR compared with both TePt NTs and pure Pt catalysts. It was concluded that alloying Pt with both Te and Cu could effectively reduce Pt d-band center owing to the electronic and geometric structure effects, which weakened the binding strength between Pt surface atoms and OH*/CO* intermediate species, and therefore improved Pt catalytic activity. Our studies provided a new alternative ternary Pt-based catalyst for both ORR and MOR, which may find application in DMFC.

## Acknowledgements

The present work was financially supported by the National Natural Science Foundation of China (21105041, 21127006, 21205056 and 21305058), Natural Science Foundation of Shandong Province (JQ201106), and Promotive Research Fund for Excellent Young and Middle-Aged Scientists of Shandong Province (BS2013CL005).

## Notes and references

*Corresponding author:*

*Phone: +86-635-8239001. E-mail address: haiboli@mail.ustc.edu.cn (H.B. Li), liujifeng111@gmail.com (J. F. Liu)

Electronic Supplementary Information (ESI) available: EDS of TeCuPt NWs before and after electrochemical dealloying (Figure S1); TEM images of TeCuPt NWs before and after KOH treatment (Figure S2); HRTEM image of TeCuPt NW (Figure S3); EDS of TePt NTs (Figure S4), TEM and HRTEM of TeCuPt (Figure S5) and TePt (Figure S6) alloys obtained by fast injection;

1 B. Lim, X. Lu, M. Jiang, P. H. C. Camargo, E. C. Cho, E. P. Lee and Y. Xia, *Nano Lett.*, 2008, **8**, 4043–4047.

2 N. Tian, Z. Y. Zhou, S. G. Sun, Y. Ding and Z. L. Wang, *Science*, 2007, **316**, 732–735.

3 L. Wei, Y. J. Fan, N. Tian, Z. Y. Zhou, X. Q. Zhao, B. W. Mao and S. G. Sun, *J. Phys. Chem. C*, 2011, **116**, 2040–2044.

4 S. Zhang, Y. Shao, G. Yin and Y. Lin, *J. Mater. Chem.*, 2010, **20**, 2826–2830.

5 Y. Li, Y. Li, E. Zhu, T. McLouth, C. Y. Chiu, X. Huang and Y. Huang, *J. Am. Chem. Soc.*, 2012, **134**, 12326–12329.

6 N. Mansor, A. B. Jorge, F. Corà, C. Gibbs, R. Jervis, P. F. McMillan, X. Wang and D. J. L. Brett, *J. Phys. Chem. C*, 2014, **118**, 6831–6838.

7 H. Meng, F. Xie, J. Chen, S. Sun and P. K. Shen, *Nanoscale*, 2011, **3**, 5041–5048.

8 D. C. Higgins, J. Y. Choi, J. Wu, A. Lopez and Z. Chen, *J. Mater. Chem.*, 2012, **22**, 3727–3732.

9 J. Yin, L. Wang, C. Tian, T. Tan, G. Mu, L. Zhao and H. Fu, *Chem. –Eur. J.*, 2013,

**19**, 13979–13986.

10 Z. Qiu, H. Huang, J. Du, X. Tao, Y. Xia, T. Feng, Y. Gan and W. Zhang, *J. Mater. Chem. A*, 2014, **2**, 8003–8008.

11 Z. Qiu, H. Huang, J. Du, T. Feng, W. Zhang, Y. Gan and X. Tao, *J. Phys. Chem. C*, 2013, **117**, 13770–13775.

12 Y. Chen, Z. Liang, F. Yang, Y. Liu and S. Chen, *J. Phys. Chem. C*, 2011, **115**, 24073–24079.

13 F. Zheng, W. T. Wong and K. F. Yung, *Nano Res.*, 2014, **7**, 410–417.

14 M. Shao, G. He, A. Peles, J. H. Odell, J. Zeng, D. Su, J. Tao, T. Yu, Y. Zhu and Y. Xia, *Chem. Commun.*, 2013, **49**, 9030–9032.

15 J. Yoon, H. Baik, S. Lee, S. J. Kwon and K. Lee, *Nanoscale*, 2014, **6**, 6434–6439.

16 K. D. Beard, D. Borrelli, A. M. Cramer, D. Blom, J. W. Van Zee and J. R. Monnier, *ACS Nano*. 2009, **3**, 2841–2853.

17 K. Zhang, Q. Yue, G. Chen, Y. Zhai, L. Wang, H. Wang, J. Zhao, J. Liu, J. Jia and H. Li, *J. Phys. Chem. C*, 2010, **115**, 379–389.

18 J. l. Shui, C. Chen and J. C. M. Li, *Adv. Funct. Mater.*, 2011, **21**, 3357–3362.

19 B. Y. Xia, H. B. Wu, X. Wang and X. W. Lou, *J. Am. Chem. Soc.*, 2012, **134**, 13934–13937.

20 Y. Qi, T. Bian, S. I. Choi, Y. Jiang, C. Jin, M. Fu, H. Zhang and D. Yang, *Chem. Commun.*, 2014, **50**, 560–562.

21 J. Wu and H. Yang, *Nano Res.*, 2011, **4**, 72–82.

22 S. Mukerjee, S. Srinivasan, M. P. Soriaga and J. McBreen, *J. Electrochem. Soc.*,

1995, **142**, 1409–1422.

23 H. H. Li, C. H. Cui, S. Zhao, H. B. Yao, M. R. Gao, F. J. Fan and S. H. Yu, *Adv. Energy Mater.*, 2012, **2**, 1182−1187.

24 C. Xu, Q. Li, Y. Liu, J. Wang and H. Geng, *Langmuir*, 2011, **28**, 1886−1892.

25 H. Zhu, S. Zhang, S. Guo, D. Su and S. Sun, *J. Am. Chem. Soc.*, 2013, **135**, 7130−7133.

26 D. Y. Wang, H. L. Chou, Y. C. Lin, F. J. Lai, C. H. Chen, J. F. Lee, B. J. Hwang and C. C. Chen, *J. Am. Chem. Soc.*, 2012, **134**, 10011−10020.

27 T. He and E. Kreidler, *Phys. Chem. Chem. Phys.*, 2008, **10**, 3731−3738.

28 R. Srivastava, P. Mani, N. Hahn and P. Strasser, *Angew. Chem. -Int. Edit.* **2007**, *46*, 8988−8991.

29 S. J. Hwang, S. J. Yoo, S. Jang, T. H. Lim, S. A. Hong and S. K. Kim, *J. Phys. Chem. C*, 2011, **115**, 2483−2488.

30 B. S. Choi, Y. W. Lee, S. W. Kang, J. W. Hong, J. Kim, I. Park and S. W. Han, *ACS Nano*, 2012, **6**, 5659−5667.

31 J. Luo, L. Wang, D. Mott, P. N. Njoki, N. Kariuki, C. J. Zhong and T. He, *J. Mater. Chem.*, 2006, **16**, 1665−1673.

32 H. H. Li, S. Zhao, M. Gong, C. H. Cui, D. He, H. W. Liang, L. Wu and S. H. Yu, *Angew. Chem. -Int. Edit.*, 2013, **52**, 7472−7476.

33 G. Xi, Y. Liu, X. Wang, X. Liu, Y. Peng and Y. Qian, *Cryst. Growth Des.*, 2006, **6**, 2567−2570.

34 P. Strasser, S. Koh, T. Anniyev, J. Greeley, K. More, C. Yu, Z. Liu, S. Kaya, D.

Nordlund, H. Ogasawara, M. F. Toney and A. Nilsson, *Nat. Chem.*, 2010, **2**, 454−460.

35 J. Yang, J. Yang and J. Y. Ying, *ACS Nano*, 2012, **6**, 9373−9382.

36 M. Wakisaka, S. Mitsui, Y. Hirose, K. Kawashima, H. Uchida and M. Watanabe, *J. Phys. Chem. B*, 2006, **110**, 23489−23496.

37 D. Briggs and M. P. Seah, *Practical Surface Analysis, 2nd Ed., Volume1: Auger and X-ray Photoelectron Spectroscopy*, 1990.

38 M. Weinert and R. E. Watson, *Phys. Rev. B*, 1995, **51**, 17168−17180.

39 G. M. Ganea, P. E. Kolic, B. El-Zahab and I. M. Warner, *Anal. Chem.*, 2011, **83**, 2576−2581.

40 I. E. L. Stephens, A. S. Bondarenko, F. J. Perez-Alonso, F. Calle-Vallejo, L. Bech, T. P. Johansson, A. K. Jepsen, R. Frydendal, B. P. Knudsen, J. Rossmeisl and I. Chorkendorff, *J. Am. Chem. Soc.*, 2011, **133**, 5485−5491.

41 S. Koh and P. Strasser, *J. Am. Chem. Soc.*, 2007, **129**, 12624−12625.

42 H. Liao and Y. Hou, *Chem. Mater.*, 2013, **25**, 457–465.

43 N. Wakabayashi, M. Takeichi, H. Uchida and M. Watanabe, *J. Phys. Chem. B*, 2005, **109**, 5836−5841.

44 F. J. Lai, H. L. Chou, L. S. Sarma, D. Y. Wang, Y. C. Lin, J. F. Lee, B. J. Hwang and C. C. Chen, *Nanoscale*, 2010, **2**, 573−581.

45 C. T. Hsieh, Y. S. Chang and K. M. Yin, *J. Phys. Chem C*, 2013, **117**, 15478−15486.

## Table and figure captions:

**Table 1.** Binding energies, chemical states, and relative intensities of Pt4f CL spectra for TeCuPt NWs, TePt NTs, and pure Pt (JM) catalysts.

**Table 2.** Comparison of ECSA, ORR activity, and MOR activity for TeCuPt NWs, TePt NTs, and pure Pt (JM) catalysts.

**Scheme 1**. Schematic illustration of the formation process for ternary TeCuPt NWs.

**Figure 1.** (a) SEM, (b, c) TEM images of the Te NWs. (d) HRTEM image of an individual Te nanowire in (c). The inset shows the corresponding electron diffraction (ED) pattern obtained from the individual Te nanowire.

**Figure 2.** XRD patterns of ternary TeCuPt NWs before (purple curve) and after (black curve) KOH treatment. The Te (JCPDS No. 36-1452), TePt (JCPDS No. 18-976) and TeCu (JCPDS No. 22-252) standard diffraction pattern were referred from PCPDFWIN (Version 2.3).

**Figure 3.** (a) XPS spectra of Pt 4f CL for TeCuPt NWs, TePt NTs, and pure Pt (JM) catalysts. The Pt 4f CL spectra for (b) TeCuPt NWs, (c) TePt NTs, and (d) pure Pt (JM) catalysts were deconvoluted into four peaks.

**Figure 4.** (a, b) TEM images of ternary TeCuPt NWs before KOH treatment. (c) SEM, (d–f) TEM, and (g, h) HRTEM images of ternary TeCuPt NWs after KOH treatment. (i) HAADF-STEM and (j-l) HAADF–STEM–EDS element mapping images for ternary TeCuPt NWs after KOH treatment.

**Figure 5.** (a, b) TEM, and (c–e) HRTEM images of TePt NTs.

**Figure 6.** CV profiles in Ar-statured 0.5 M $H_2SO_4$ solution for (a) TeCuPt NWs and (b)

pure Pt (JM) catalysts during the electrochemical dealloying process (along the arrow the curves correspond to: 1st, 5th, 10th, 20th, 30th, 50th, 150th, 250th cycle) (sweeping rate: 0.5 V/s).

**Figure 7.** (a) TEM and (b–d) HRTEM images of TeCuPt NWs after dealloying. (e) HAADF-STEM and (f–h) HAADF-STEM-EDS element mapping images for a representative TeCuPt NW after dealloying. (i) Te, Cu, and Pt element profiles along the line across the TeCuPt NW shown in (e).

**Figure 8.** (a) CV profiles of TeCuPt NWs, TePt NTs, and pure Pt (JM) catalysts in Ar-saturated 0.5 M $H_2SO_4$ (sweep rate: 0.5 V/s). (b) LSVs of TeCuPt NWs, TePt NTs, and pure Pt (JM) catalysts in $O_2$-saturated 0.05 M $H_2SO_4$ (sweep rate: 10 mV/s, 1600 rpm). (c) Tafel plots of TeCuPt NWs, TePt NTs, and pure Pt (JM) catalysts for ORR at high potential range. (d) Specific kinetic mass ($J_{mass}$) and area ($J_{area}$) activities of TeCuPt NWs, TePt NTs, and pure Pt (JM) catalysts for ORR at 0.83 V *vs.* RHE.

**Figure 9.** (a) Mass-normalized CV profiles (sweep rate: 20 mV/s) and (b) CA curves for methanol oxidation on TeCuPt NWs, TePt NTs, and pure Pt (JM) catalysts in Ar-saturated 0.50 M $H_2SO_4$ + 1.0 M $CH_3OH$. The CA curves were obtained at 0.8 V *vs.* RHE.

**Table 1.**

| Catalyst | Binding energy Pt 4f 7/2 (eV) | Binding energy Pt 4f 5/2 (eV) | Chemical state | Relative intensity (%) |
|---|---|---|---|---|
| TeCuPt | 71.3 | 74.6 | Pt(0) | 77.9 |
| | 72.4 | 75.8 | Pt(II) | 22.1 |
| TePt | 71.1 | 74.4 | Pt(0) | 76.5 |
| | 72.1 | 75.5 | Pt(II) | 23.5 |
| Pt(JM) | 70.6 | 73.9 | Pt(0) | 74.1 |
| | 71.6 | 74.7 | Pt(II) | 25.9 |

**Table 2.**

| Catalyst | ECSA | MOR | | | ORR | | |
|---|---|---|---|---|---|---|---|
| | ($m^2/g_{Pt}$) | $E_f$ (V) | $J_f$ ($mA/mg_{Pt}$) | $J_f/J_b$ | $E_{1/2}$ (V) | $J_{area}$[a] ($mA/cm^2_{Pt}$) | $J_{mass}$[b] ($mA/mg_{Pt}$) |
| TeCuPt | 20.1 | 0.85 | 245 | 1.10 | 0.83 | 0.29 | 59 |
| TePt | 15.5 | 0.87 | 223 | 1.00 | 0.82 | 0.25 | 44 |
| Pt(JM) | 14.2 | 0.87 | 105 | 0.90 | 0.80 | 0.11 | 16 |

*a,b: Potential was fixed at 0.83 V vs. RHE.*

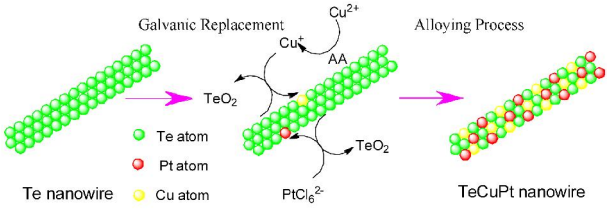


**Scheme 1.**

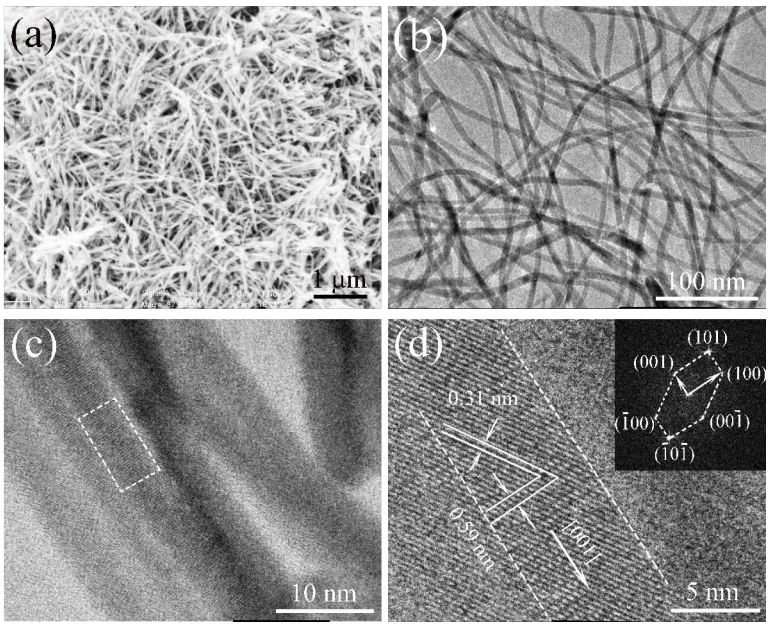


Figure 1

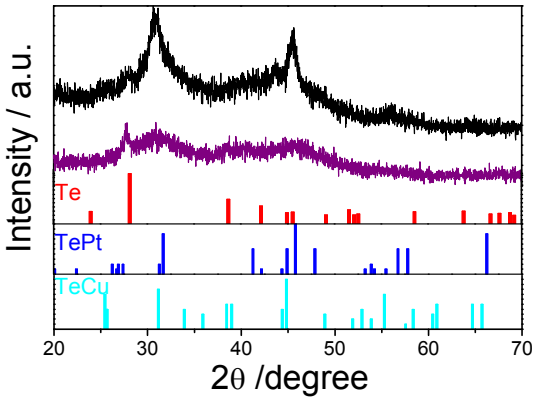


Figure 2

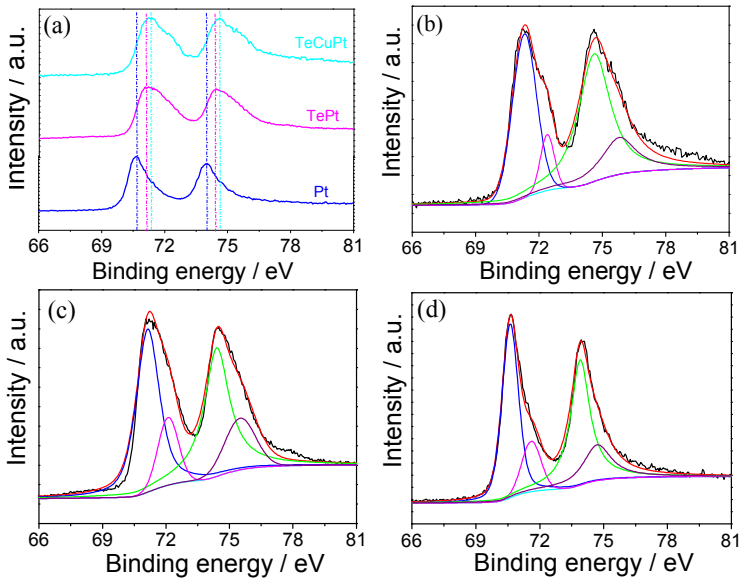


Figure 3

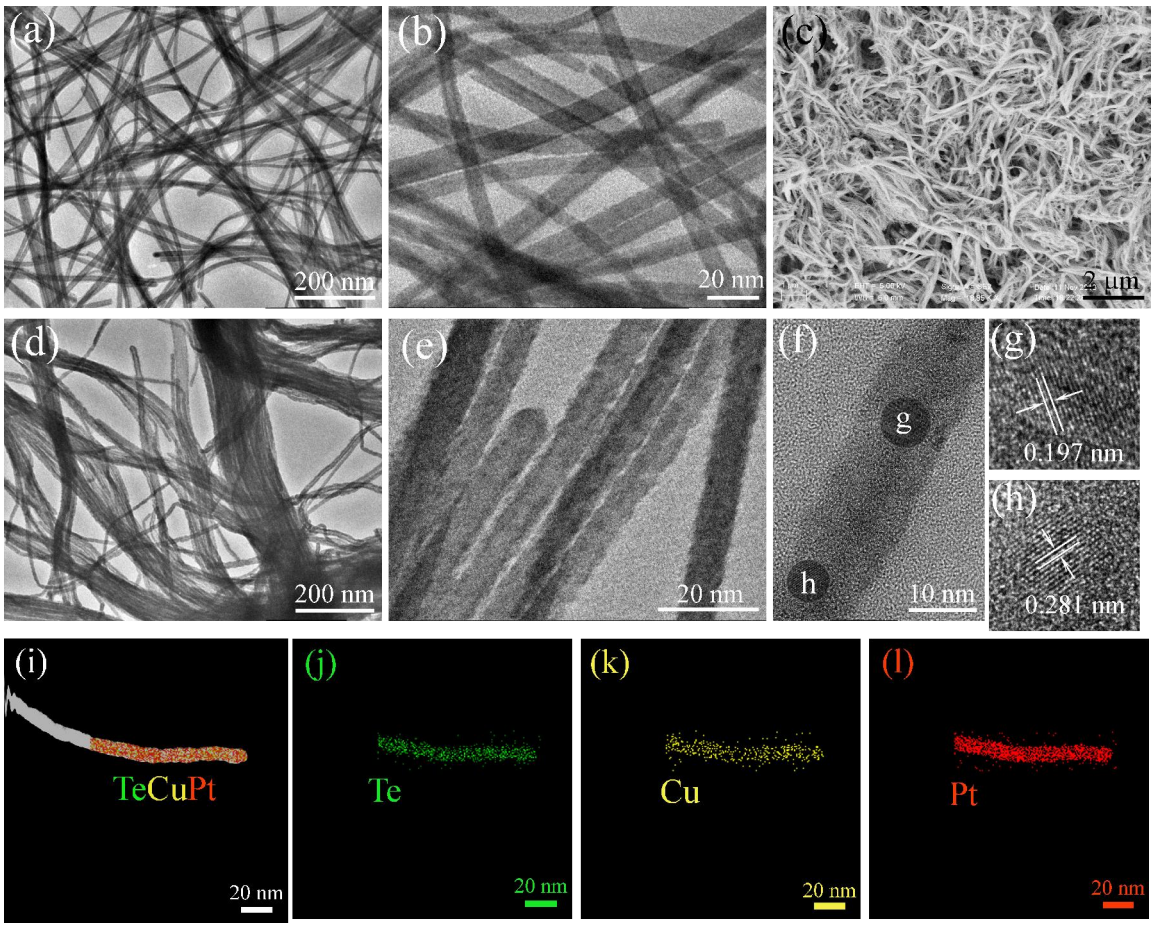


Figure 4

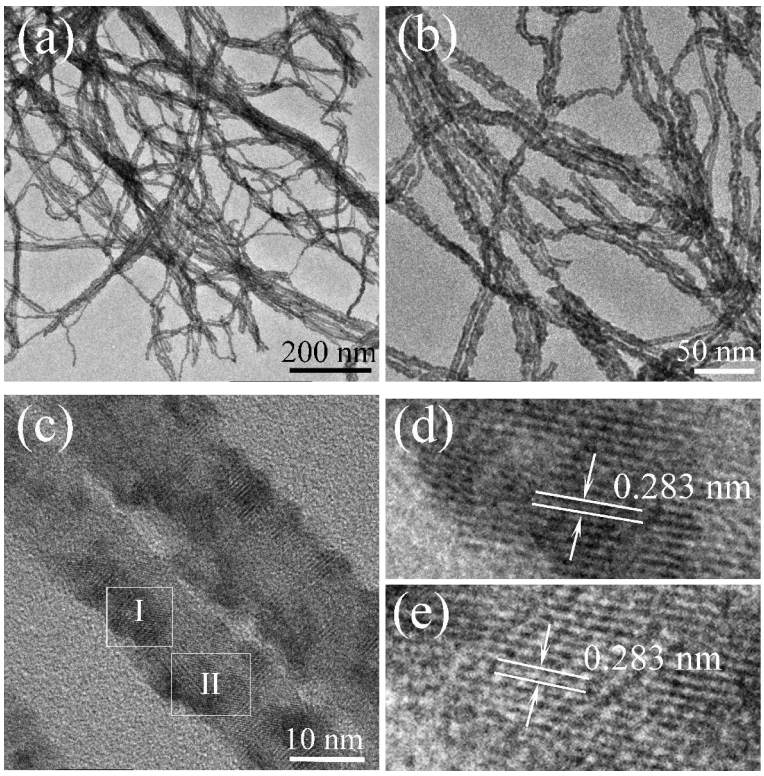


Figure 5

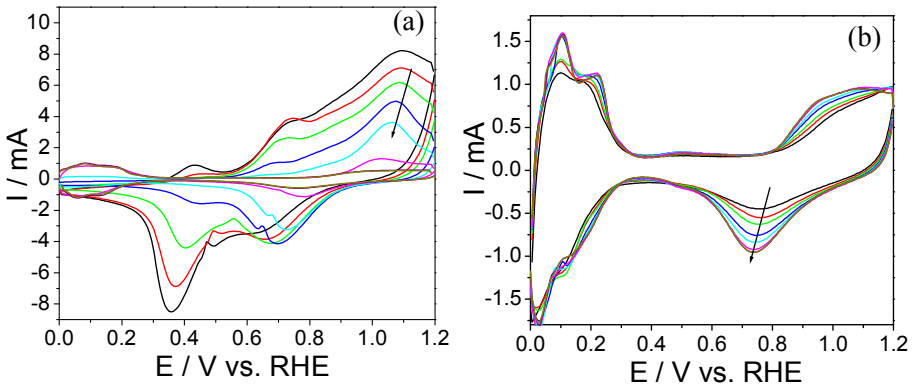


Figure 6

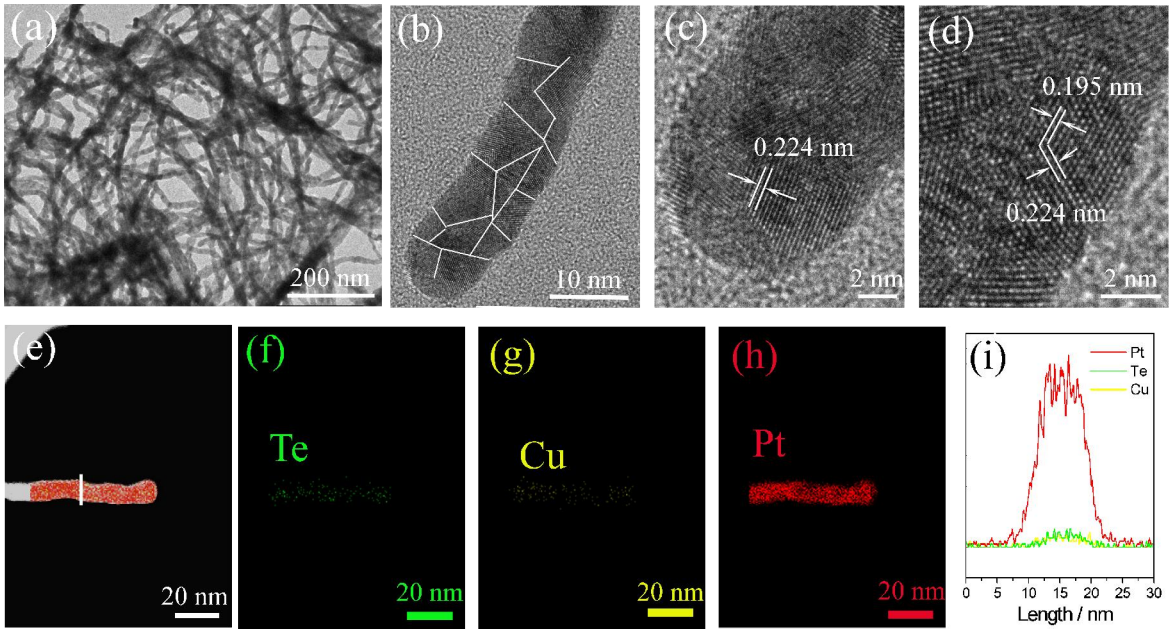


Figure 7

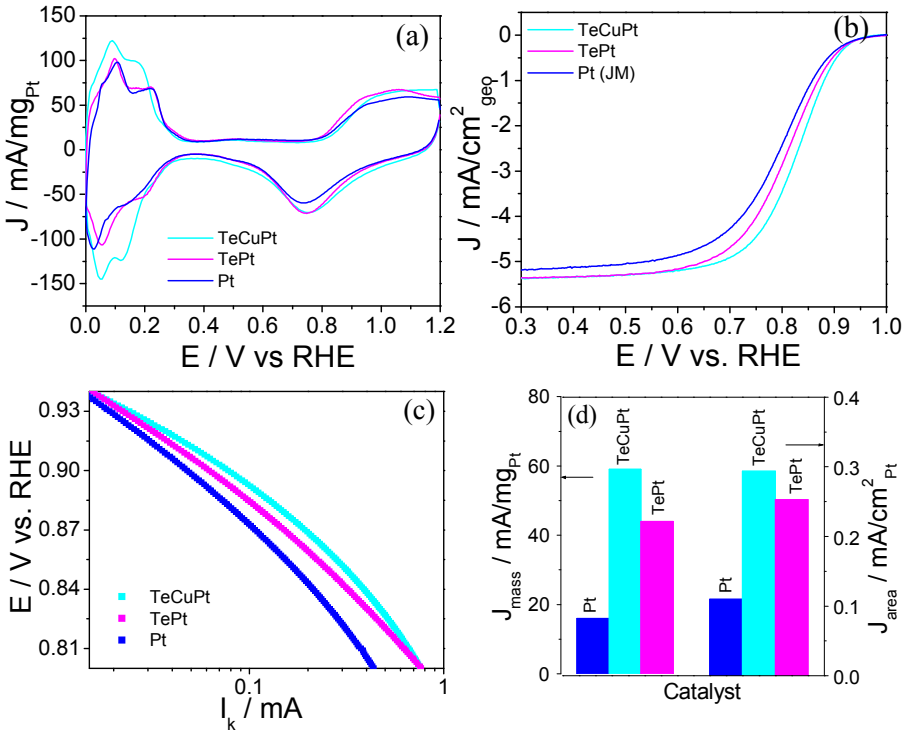


Figure 8

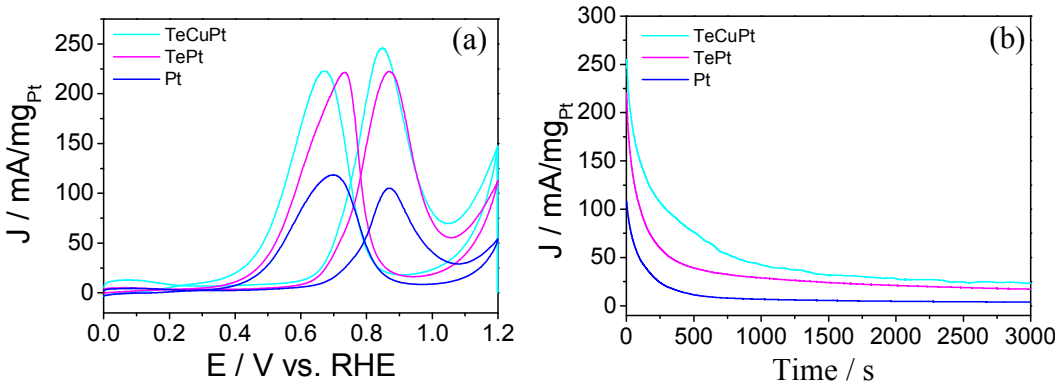


Figure 9